Microgravity Burner-Generated Spherical Diffusion Flames: Experiment and Computation

STEPHEN D. TSE,[†] DELIN ZHU, CHIH-JEN SUNG,[†] YIGUANG JU,[§] and CHUNG K. LAW*

Department of Mechanical and Aerospace Engineering, Princeton University, Princeton, NJ 08544, USA

Microgravity experiments were conducted in the 2.2-s drop-tower facility at the NASA Glenn Research Center to study the transient response of the burner-generated spherical diffusion flame caused by its initial displacement from the steady-state position. The experiment involved issuing H_2/CH_4/inert mixtures of constant fuel mass flow rates from a bronze, porous, 1.27-cm-diameter, spherical burner into atmospheric air. The experimental results on the flame trajectory were found to agree well with those obtained through fully transient computational simulation with detailed chemistry and transport, and appropriate initial conditions. Furthermore, although steady-state behavior should exist for such flames, the experimental and computational results indicated that it cannot be reached within the 2.2-s microgravity duration for the fuels and mass-flow rates tested.

To assess the role of radiation on the flame dynamics and extinction, computations were performed without radiation, with radiation employing the optically thin approximation, and with radiation utilizing a detailed emission/absorption statistical narrow band (SNB) model. The computation showed that while the influence of radiative heat loss on the position of the flame is small, proper consideration of radiative effects is crucial in assessing the state of flame extinction. Specifically, while all simulations of the experimental cases studied incorporating radiative heat loss revealed that the flame extinguishes well before the attainment of steady state, simulations accounting for gaseous reabsorption of radiative emissions were required to adequately represent the experiments in terms of extinction time, with the optically thin simulations predicting premature extinction during the flame expansion process. Effects of heat loss to the porous burner were also examined, and the lack of correspondence between the visible flame luminosity and flame strength, as related to flame temperature and heat release rate, was noted.

INTRODUCTION

The presence of buoyant flows on earth can significantly modify and complicate the convective-diffusive transport processes needed to mix and heat the fuel and oxidant reactants before chemical reaction can be initiated. In particular, the uni-directional nature of the gravity vector frequently introduces a degree of asymmetry into an otherwise symmetric phenomenon. As such, the resulting complex, multi-dimensional flame configuration not only causes substantial difficulties in experimentation and consequently compromises the quality and fidelity of the data generated, it can also impose limitations on theoretical developments either analytically or computationally. This situation renders direct comparison between theory and experiments either difficult or meaningless.

Extensive microgravity experiments on diffusion flames have been conducted with droplet combustion. While such experiments are of value in their own right, the small dimension and the intrinsic unsteadiness impose complications for their usefulness in flame structure studies. These difficulties can be circumvented with the steady-state, burner-generated spherical diffusion flames of gaseous reactants. Specifically, the state of the gaseous-fuel mixture supplied to the burner is well defined and controllable, and hence the flame as well, rendering the configuration ideal for fundamental study. For example, by issuing gaseous fuel from the burner, the state of flame extinction can be easily identified as the fuel-flow rate for which a steady flame does not exist. Experimentally, Atreya and collaborators [1, 2] and Axelbaum and collaborators [3] have utilized spherical burner-stabilized gaseous diffusion flames to

*Corresponding author. E-mail: cklaw@princeton.edu

[†]Currently at Department of Mechanical and Aerospace Engineering, Rutgers, the State University of New Jersey, Piscataway, NJ 08854.

[‡]Currently at Department of Mechanical and Aerospace Engineering, Case Western Reserve University, Cleveland, OH 44106.

[§]Currently at Department of Engineering Mechanics, Tsinghua University, Beijing 100084, China.

COMBUSTION AND FLAME 125:1265–1278 (2001)

Published by Elsevier Science Inc.

0010-2180/01/$–see front matter
PII S0010-2180(01)00247-4

investigate the associated processes of sooting and radiation. Analytically, Matalon and collaborators [4, 5] have investigated the structure and extinction characteristics of burner-generated spherical diffusion flames.

The present research endeavor is the first phase of a long-range program on the study of the structure and response of diffusion flames via the one-dimensional, spherically symmetric geometry generated by ejecting fuel from a porous spherical burner into a stagnant oxidizing environment. There are several objectives underlying the present investigation. First, we explore the feasibility that spherical diffusion flames of good quality can indeed be experimentally established in a microgravity environment. Second, we assess the relaxation time required for the flame to reach steady state; this information is needed to decide on the specific microgravity facility that is most appropriate to conduct further experimentation. Third, we conduct a parallel computational simulation of the experimentation with detailed chemistry and transport. The present state of the art on laminar flames with simple configuration and flow field demands a good agreement between experiment and computation when they are both conducted correctly. If such an agreement does exist, then the computed results can be used to provide further information on the flame dynamics and structure that are not readily obtainable from the microgravity experimentation. Indeed, we shall demonstrate that our computational results provide useful evidence and insight into such issues as radiative extinction and flame luminosity.

In the present investigation, microgravity experiments were performed in the NASA-Glenn 2.2-s drop tower facility, with the experimental transient response attained through an impulsive step from normal-gravity to microgravity conditions. We shall show in due course that while combustion does seem to approach steady state, the relaxation process involving the flame movement can be exceedingly long, requiring microgravity experimentation of extended duration. The experimental and computational specifications and results are respectively presented in the next two sections, with comparison between them conducted in parallel when discussing the computational results.

EXPERIMENT

Experimental Specifications

The experiments were conducted in the 2.2-s drop-tower facility at NASA Glenn Research Center [6], employing the combustion apparatus shown in Fig. 1. The experiment was contained in a standard aluminum drop-rig frame. The top of the chamber was open to atmospheric air, ensuring a constant pressure condition, as well as plentiful oxidizer supply. The drop package was comprised of a porous spherical burner, an ignition system, a gas-flow system, pressure transducers, imaging equipment, thermocouples, and a computerized data acquisition and storage system. System power was provided by on-board battery packs.

Fuel mixtures were issued radially from a bronze porous spherical burner (5-μm average pore diameter, 1.27-cm sphere diameter) into atmospheric air. The burner consists of bronze beads diffusionally bonded within a spherical mold. The uniformity of the outgoing flow is assessed based on the sphericity of the resultant microgravity flame, within a specified flow rate. Ignition was accomplished in normal-gravity, prior to drop, by a hot-wire coil mounted onto a retractable rotary solenoid. The burner was supported by a stainless-steel tube (1.5-mm o.d.) through which gas was fed to the burner. The flow system consisted of two supply lines to the burner, running in parallel from a 3-liter mixture cylinder, containing fuel and inert (at $\sim$7 atm). Each supply line was flow-regulated by a critical (sonic) nozzle and was controlled by a solenoid valve. In general, each line was metered to a different flow rate so that different total flow rates, via line combinations, could be delivered to the burner during the course of a single experimental drop. Stagnation pressures upstream of the critical nozzles were pre-set by regulator valves and monitored by pressure transducers. The volumetric flow rates ranged from about 10 to 30 mL/s. The visible flame image was recorded onto an S-VHS tape with a high-resolution color CCD camera. Relative times (hours:minutes:seconds:frames) were stamped onto the video data, recorded at 30 frames per second, with a synchronized time-code generator. The burner was not actively

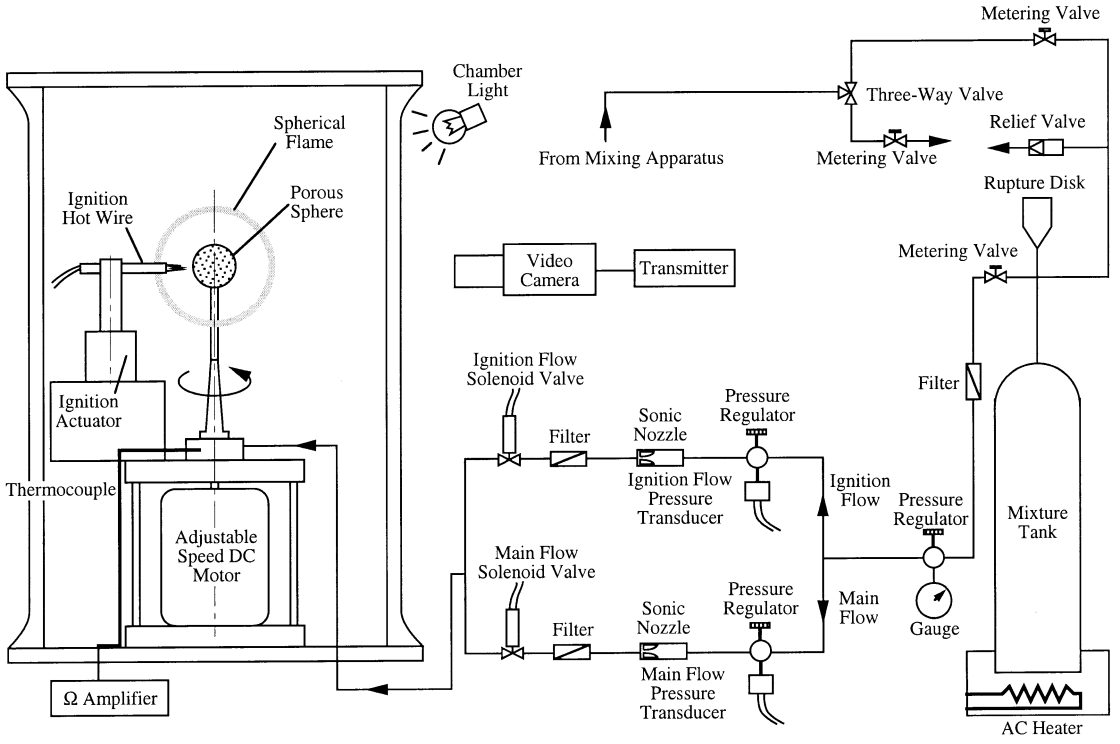

Fig. 1. Schematic of spherical diffusion flame drop package combustion apparatus.

cooled because of its small size and the limited experimental duration. The burner surface and the ambient temperatures were measured by 0.0762-mm diameter K-type thermocouples.

Experiments were performed by using fuel mixtures with different species concentrations of H_2, CH_4, and N_2, burning in atmospheric air for different mass flow rates. All mixtures were diluted with at least 40% nitrogen to reduce the flame size and the transient time, for optimal adaptation to the experimental confinement and duration. Hydrogen was selected for its non-sooty nature and favorable ignition characteristics. However, because of the low visible luminosity of hydrogen, methane was added to visualize the flame. Previous experiments with nitrogen-diluted methane mixtures revealed that while ignition was difficult with less than 30% methane, the flames tended to soot with higher concentrations, hence destroying the spherical flame shape as observed previously in Ref. 1. Consequently, fuel mixtures were chosen and varied to maximize flame luminosity and sphericity (to be defined later), and at the same time to minimize flame size and transient time.

Experimental Results

The quality of the spherical diffusion flames produced by the porous-sphere burner in the drop-tower experiments is excellent, as evinced in the photographs of the representative experiment of Fig. 2. For all of the experiments, the mixture was ignited about 1 s before drop, so that a "steady" normal-gravity flame could be established. It is seen that, at the moment of drop, the flame is teardrop-shaped, Fig. 2a, but rapidly becomes spherical and expands outwardly, away from the burner, under the newly imposed microgravity condition, Fig. 2b–d. For this particular experiment (50% H_2/10% CH_4/40% N_2 mixture, 8.1 mg/s mass-flow rate), the flame possesses ~1.0 sphericity and 0.94 concentricity at 0.5 s into microgravity, as shown in Fig. 2c; with sphericity and concentricity being, respectively, defined as the ratio of the horizontal and the vertical diameters of the flame and as the distance between center of the burner and bottom of the flame divided by half of the vertical diameter of the flame [7].

Data for the flame radii as a function of time,

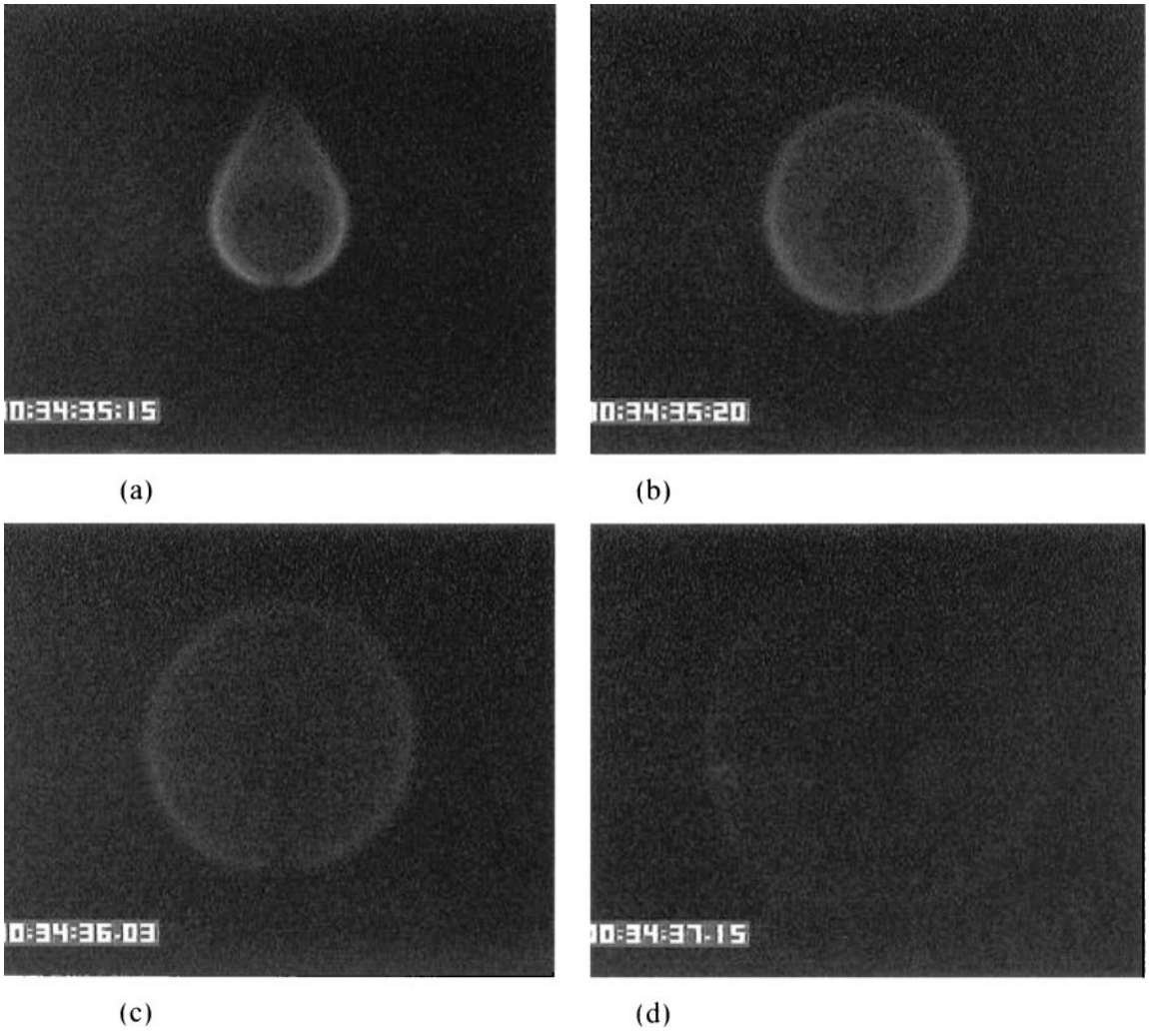

Fig. 2. Spherical diffusion flame images from drop tower. Fuel mixture composition: 50%H_2-10%CH_4-40%N_2. Mass-flow rate: 8.1 mg/s. Time into microgravity: (a) 0.0 s; (b) 0.166 s; (c) 0.6 s; (d) 2.0 s.

for some of the experiments, are shown in Fig. 3. The measured experimental values of the flame radii correspond to the outer edge of the faint blue region of the flames. Case (i), as designated by shaded diamonds of Fig. 3, corresponds to the photographs of Fig. 2. As expected, larger radii correspond to larger mass flow rates for a given fuel mixture. The steady growth of the flames resembles earlier experimental results on the temporal variation of the flamefront standoff ratio for droplet combustion in micro-buoyancy [8, 9], exhibiting the influence of fuel vapor accumulation.

After the spherical flame is established, the temperature of the burner surface is found to range from 350 to 390 K for the various fuel mixtures. It is of particular interest to note that all experimental images show that the visible luminosity of the flame decreases remarkably with increasing time, as demonstrated in Fig. 2.

COMPUTATIONAL SIMULATION

Computational Specifications

The experimental situation was computationally simulated by using the Sandia burner-stabilized premixed flame code [10], with detailed chemical, transport, and (optically thin and optically

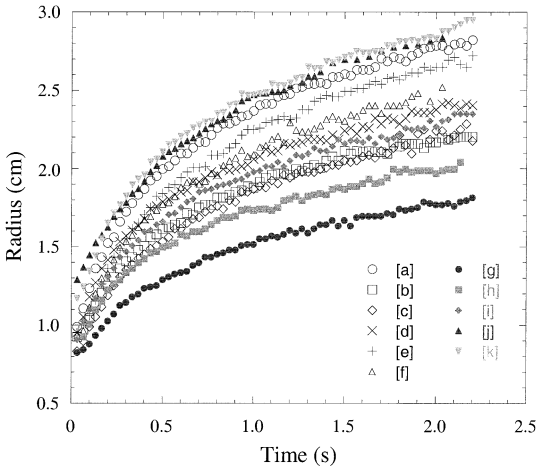

Fig. 3. Data of flame radii as a function of time for various cases. *20%H_2-25%CH_4-55%N_2*: [a] 15.72 mg/s. *25%H_2-20%CH_4-55%N_2*: [b] 10.55 mg/s. *30%H_2-15%CH_4-55%N_2*: [c] 9.42 mg/s, [d] 12.0 mg/s, [e] 15.31 mg/s. *40%H_2-10%CH_4-50%N_2*: [f] 12.37 mg/s. *50%H_2-10%CH_4-40%N_2*: [g] 4.96 mg/s, [h] 6.43 mg/s, [i] 8.1 mg/s, [j] 1.67 mg/s, [k] 13.03 mg/s.

thick) radiation models, along with appropriate modifications to include transient terms in the mass, species, and energy conservation equations, and with boundary conditions for nonpremixed burning. By using the small Mach number approximation, where the thermodynamic pressure is constant throughout the flow field, the governing equations are:

$$A\frac{\partial \rho}{\partial t} + \frac{\partial m}{\partial r} = 0, \tag{1a}$$

$$\rho A\frac{\partial T}{\partial t} + \dot{m}\frac{\partial T}{\partial r} - \frac{1}{c_p}\frac{\partial}{\partial r}\left(A\lambda\frac{\partial T}{\partial r}\right) + \frac{A}{c_p} \cdot \sum_{k=1}^{K} \rho Y_k V_k c_{p_k}\frac{\partial T}{\partial r} + \frac{A}{c_p} \cdot \sum_{k=1}^{K} \dot{\omega}_k h_k W_k + \frac{A}{c_p}\dot{q}_{rad} = 0. \tag{1b}$$

$$\rho A\frac{\partial Y_k}{\partial t} + m\frac{\partial Y_k}{\partial r} + \frac{\partial}{\partial r}(\rho A Y_k V_k) - A\dot{\omega}_k W_k = 0, \tag{1c}$$

where $A = 4\pi r^2$, r is the radius, m the mass-flow rate, T the temperature, c_p and λ the constant-pressure heat capacity and thermal conductivity of the mixture, respectively, and K the total number of species. Furthermore, Y_k, W_k, $\dot{\omega}_k$, h_k, and V_k are the mass fraction, the molecular weight, the molar chemical production rate per unit volume, the specific enthalpy, and the diffusion velocity of the kth species, respectively, while $\dot{q}_{rad}$ is the radiative heat-loss rate per unit volume.

For the optically thin radiation simulations, the approach of Ref. 11 was employed such that

$$\dot{q}_{rad} = 4\alpha_p\sigma(T^4 - T_\infty^4), \tag{2}$$

where σ is the Stefan–Boltzmann constant and α_p the total Planck mean absorption coefficient. Radiative heat loss was considered to be emitted only from the reactant, CH_4, and the combustion products, CO_2, H_2O, and CO. Planck mean absorption/emission coefficients of Tien [12] and Hubbard and Tien [13], based on a wide-band model, were compared to those of Ju et al. [14] based on a statistical narrow-band model.

For the optically thick radiation studies, radiative transport including both emission and absorption was computed by using the statistical narrow-band (SNB) model with exponential-tailed inverse line strength distribution [15]. The radiative transfer equations were solved for wave-numbers between 150 and 9300 cm^{-1} with 25 cm^{-1} resolution using the S6 discrete ordinate method. Radiation parameters for CO_2, H_2O, and CO were taken from Ref. [16]. CH_4 radiation was not included because the necessary spectral data were not available, but CH_4 radiation was found to be minimal even for optically thin conditions.

At the burner surface, the boundary conditions imposed were a fixed mass flow rate m_F, temperature T_s, mass flux fractions $Y_k = \epsilon_k/(1 + \rho V_k A/m_F)$, where ϵ_k is the mass fraction of the kth species of the initial mixture, and radiative emissivity of 1. At the ambience side, the boundary conditions imposed were temperature T_∞, composition of air (21% O_2/79% N_2), and radiative emissivity of 1.

The reaction mechanism used was based on GRI-Mech 1.2 [17], which consists of 32 species and 177 elementary reaction steps, and was specifically developed and optimized for natural gas (CH_4, C_2H_6) combustion. Chemilumines-

cence intensity of the electronically excited CH species (CH*) was assumed to correspond to the bluish luminescence (~430 nm) observed in the experiments. Additional reactions (R1–R7) to predict CH* were included in the mechanism, with their rate constants taken from the corresponding references [18–22]. CH* is produced primarily from:

(R1) $C_2H + O_2 \rightarrow CH^* + CO_2$ Ref. [18]

(R2) $C_2 + OH \rightarrow CH^* + CO.$ Ref. [19]

In considering one of the main routes (R2) of CH* formation, reactions leading to C_2 formation were included:

(R3) $C_2H + HCO_2 \rightarrow +C_2 + H_2$ Ref. [20]

(R4) $CO + CO \rightarrow C_2 + O_2.$ Ref. [20]

CH* may disappear by the quenching steps:

(R5) $CH^* + M \rightarrow CH + M$ Ref. [21]

(R6) $CH^* + O_2 \rightarrow CH + O_2,$ Ref. [21]

and by photon emission:

(R7)

$CH^* \rightarrow CH + h\nu,$ Ref. [22]

where h is the Planck's constant, ν the emission frequency, and M the collision partner. While the thermodynamic properties of CH* were obtained from those of the ground-state CH, by adding the energy difference between the two to the heat of formation of the former [18, 23], the transport properties assigned to CH* are those of CH [23]. The photon emission rate per unit volume from CH* chemiluminescence can be computed as k_7[CH*], where k_7 is the rate constant of reaction (R7), and [CH*] the concentration of CH*. Visible radiation heat loss from the chemiluminescent species CH* was considered negligible.

The program solves these conservation equations of mass, energy, and species by using finite difference approximations, with adaptive gridding in space. To ensure convergence, the discretization in both time and space is reduced until no change is observed in the solution. Calculations were performed in the physical-coordinate system. The fuel mass flow rate m_F and burner surface temperature T_s were specified by those measured experimentally, and the ambient temperature T_∞ was fixed at 300 K while the ambient pressure was 1 atm. The computational domain for both the transient and the final steady-state solutions was 200 cm, which is about forty times the largest flame radius based on steady-state calculations, obtained by employing the computational methodology described above but omitting the transient terms in the governing equations. The gradients were found to be negligibly small at the finite boundary of such a domain. It is worth noting that the solutions produced by running the transient code for extended times (~3000 s) approached the solution given by the steady-state code.

The initial conditions considered in the numerical simulation are based on the experimental ignition condition. Specifically, in normal gravity, just before the experimental drop at $t = 0$, a boundary layer produced by the strong buoyant flow surrounds the porous sphere, as manifested by the flame shape of Fig. 2a. At the moment of the drop, the tear-shaped flame almost immediately becomes spherical with a single flame standoff distance which is near, but slightly larger than that at the stagnation and lateral sides for the earlier normal-gravity flame. With the gradients presumably still confined to a thin region near the sphere (for the stagnation to lateral flame locations), the flame structure there should be very localized, with negligible influence on most of the flow field encompassing it. Working from this premise, the initial flame structure is approximated by that calculated by the steady-state code with a "squeezed" domain, with the calculated position of the peak CH* concentration equivalent to the horizontal flame position experimentally observed at $t = 0$. Data points with the ambient boundary condition are then affixed, extending the domain to 200 cm. Figure 4 presents the initial flame structure condition used to simulate the flame of Fig. 2. Further calculations revealed that the transient process is not sensitive to the specific local flame structure employed, as long as the structure itself is well localized at the experimental initial flame position with respect to the entire flow field.

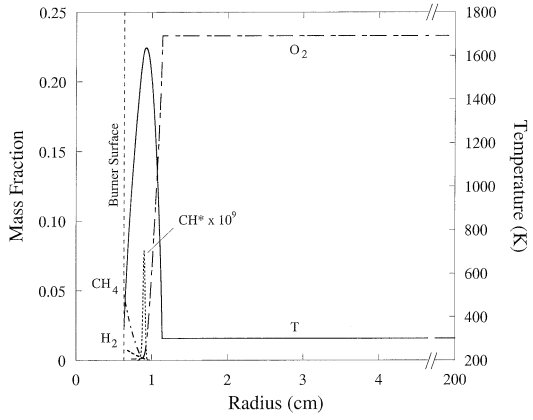

Fig. 4. Prescribed initial flame structure to simulate flame of Fig. 2 (50%H_2-10%CH_4-40%N_2, 8.1 mg/s).

Results and Discussion

Flame Trajectory

The fully transient calculations with detailed chemistry and transport agree well with the experimental data for the flame trajectory, as seen in Fig. 5, which corresponds to the representative experiment of Fig. 2. All of the other experiments given in Fig. 3 are simulated to approximately the same degree of agreement for flame trajectory, but are not presented in the format of Fig. 5 because of space limitation. Note that the term "standoff distance" used in the text and figures corresponds to the distance away from the surface of the porous burner.

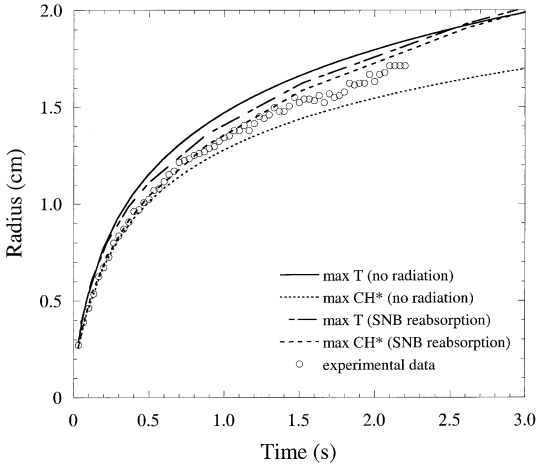

Fig. 5. Fully transient calculations and experimental data for flame of Fig. 2 (50%H_2-10%CH_4-40%N_2, 8.1 mg/s). Calculated steady-state Max T radius is 4.72 cm.

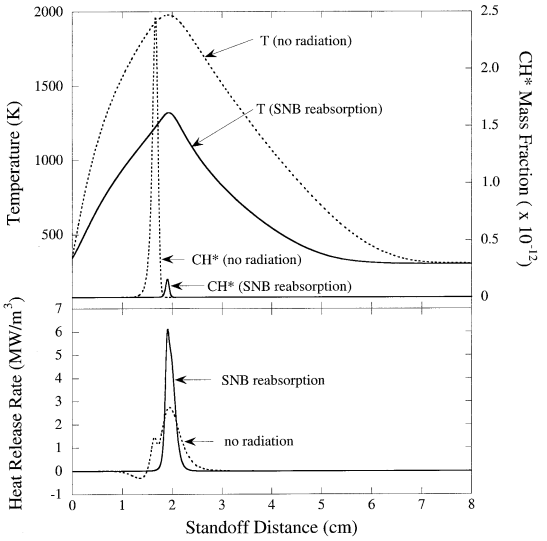

Fig. 6. Flame structure comparison of non-radiative and SNB optically thick cases at same time (2.5s) and Max T location, corresponding to Fig. 5 (50%H_2-10%CH_4-40%N_2, 8.1 mg/s).

Figure 5 shows that, for the simulations without radiative effects, the predicted instantaneous locations of peak temperature (Max T) are noticeably larger than those of peak photon emission from the CH* species (Max [CH*]), with the visible bluish flame data correlating well with the peak local luminosity from CH*. For the simulations with radiative heat losses, for both optically thin and thick cases, predicted instantaneous locations of Max T and Max [CH*] are in close proximity with each other as well as with the experimental data. This difference in the separation distance between Max T and Max [CH*] locations, for the non-radiative and radiative cases, can be attributed to the effects of heat loss on the flame structure, as demonstrated in Fig. 6, which compares the pertinent differences in flame structure for these two cases for the same time (2.5 s) and approximate flame position (Max T position). The significantly reduced temperature of the radiative case narrows the flame structure and spatially confines the highly temperature-dependent reaction zone to a thinner region, resulting in the close proximity of Max T and Max [CH*] locations. In other words, the "high" temperature region of the adiabatic flame is much wider than that of the radiative flame; as a result, peak CH* is closer to Max T for the

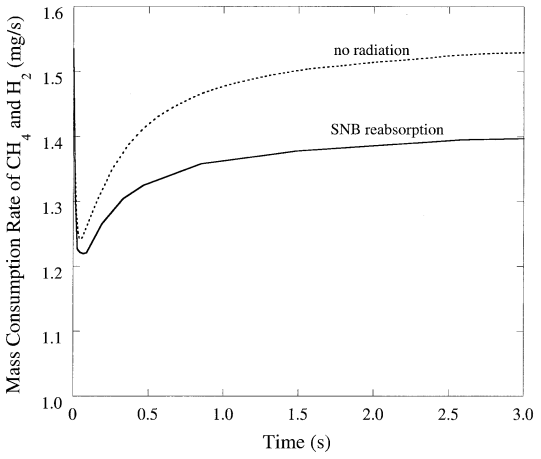

Fig. 7. Comparison of mass consumption rate for non-radiative and SNB optically thick cases, corresponding to Fig. 5 (50%H_2-10%CH_4-40%N_2, 8.1 mg/s).

radiative case. In addition, the spatial range with temperature higher than the critical temperature responsible for CH* formation is much narrower in the radiative case, because of the reduction in maximum temperature. The slight disparity of the flame trajectories between the non-radiative and radiative cases can be explained in terms of the effects of finite-rate reactions and thermal expansion. As can be seen from Fig. 7, the mass consumption rate for the radiative case is always smaller than that for the non-radiative case, due to the reduced reaction rates from reduced temperatures. Here, mass consumption is defined as the spatially integrated mass loss rate of CH_4 and H_2. However, the computations reveal that there is no reactant leakage (until the brief period just preceding flame extinction) for the radiative case despite the smaller mass consumption rate. This phenomenon is readily explained because the flame with radiative loss is able to accumulate more fuel mass for the same volume as compared to the non-radiative case, due to increased gas density from reduced temperature. As a result, during the beginning stage of flame expansion, the radiative flame is able to maintain a smaller radius with a smaller mass consumption rate and no reactant leakage. However, as the flame continues to expand and decrease in temperature, the effect of enhanced mass storage ability cannot compensate for that of decreasing reaction rates, driving the flame to move outwardly faster than in the non-radiative case in order to reduce the fuel mass flux into its consumption zone. Eventually, the heat loss brings down the flame temperature to the point of substantial reactant leakage, leading to flame extinction. The details related to radiative extinction, specifically with regard to optically thin and thick models, will be discussed later. Nonetheless, the quantitative differences in flame location predictions between the non-radiative and radiative simulations are not significant, suggesting that radiation is not the dominant factor in determining the flame position for the transient expansion process. This result is attributable to the constant fuel-mass supply rate from the burner, which, unlike the droplet problem, is unaffected by the heat flux to the burner.

Radiative Effects and Extinction

For the case of Fig. 5, extinction is predicted to occur well beyond the experimental duration of 2.2s. However, for fuel mixtures with relatively lower H_2 and higher CH_4 concentrations, optically thin computations predict extinction while the experimental flame is still extant and expanding, as shown in Fig. 8. As expected, Tien's wide-band Planck mean absorption coefficients overpredict radiative loss compared to the SNB mean coefficients for the optically thin cases. Nonetheless, only with the treatment of gas-phase self-reabsorption effects, as with utilization of the SNB model, are the computations able to describe better the experimental observations, where the flame survives for the entire 2.2-s experimental duration.

Figure 9a shows some aspects of the flame structure related to radiative effects for the reabsorption flame of Fig. 8 at an instant in time (2s). Figure 9b shows an enlarged view of the reactive-radiative region, along with the calculated radiative heat loss without reabsorption but determined by using temperature and species data obtained with reabsorption, to assess the quantitative reduction in net heat loss because of reabsorption. With reabsorption, the radiative loss rate is negative at some locations, for example, around 0–1 cm and 4–5 cm standoff distance, because some radiation emitted at high temperatures is reabsorbed at lower tem-

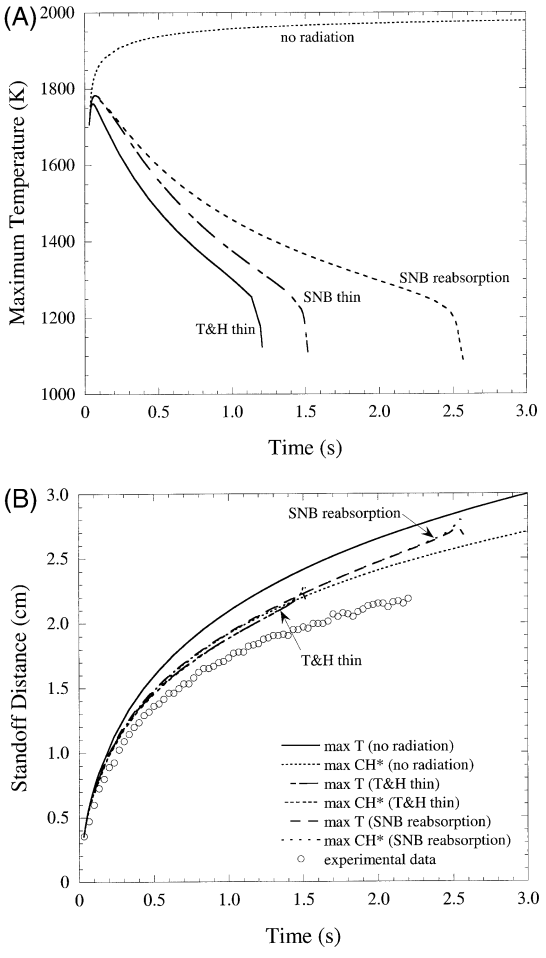

Fig. 8. Fully transient calculations and experimental data for flame of case [a] of Fig. 3 (20%H_2-25%CH_4-55%N_2, 15.72 mg/s).

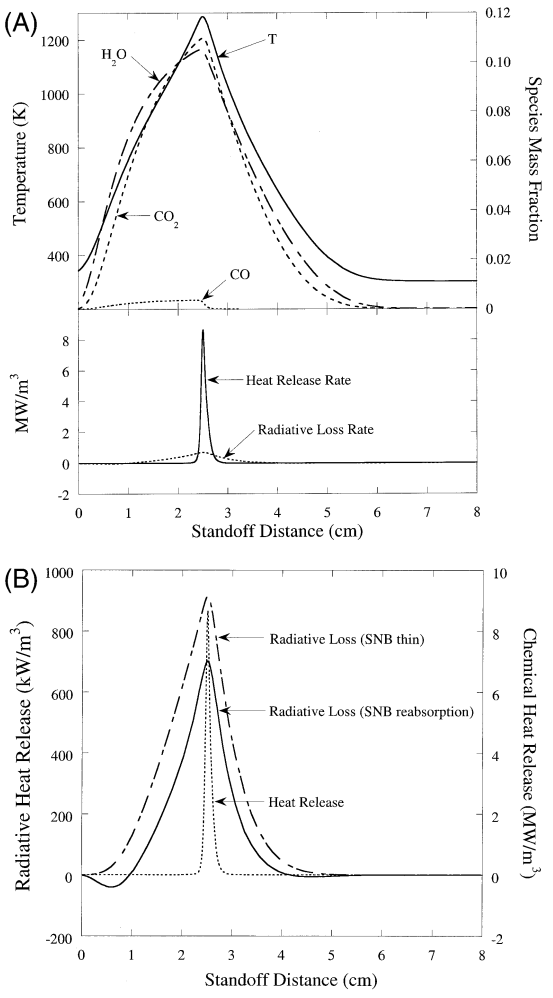

Fig. 9. (a) Flame structure aspects of SNB optically thick case of Fig. 8 (20%H_2-25%CH_4-55%N_2, 15.72 mg/s). (b) Enlarged view of reaction zone area, with radiative loss calculations assuming optically thin.

peratures. This effect reduces the net loss and preheats the fuel and oxidizer moving toward the reaction zone, increasing the flame temperature. At the same time, the dramatic reduction in the heat loss structure near the reaction zone indicates that significant amounts of reabsorption are occurring where temperatures and radiative product concentrations are high. With the mean Planck lengths for absorption for the radiative species CO_2 and H_2O (at 1000 K and 1 atm) being around 4 cm and 20 cm, respectively, one employing such a criterion would erroneously evaluate the role of radiative reabsorption in this narrow region as being negligible. Of course, the path lengths available for reabsorption are increased for the 1-D spherical flame versus the planar flame due to the symmetric geometry. Nonetheless, only with an SNB model can the physics be properly captured, where adjacent gases, due to the closely overlapping absorption/emission bands, readily absorb radiation emitted at high temperature regions. The weakness of using mean Planck lengths to assess reabsorption effects has also been shown and discussed in detail in Ref. [24].

As seen in the peak temperature history of Fig. 8, the temperature reduction because of radiative loss is remarkably drastic. However, as mentioned previously, reactant leakage resulting in flame extinction does not occur until the very end. As long as the temperature remains

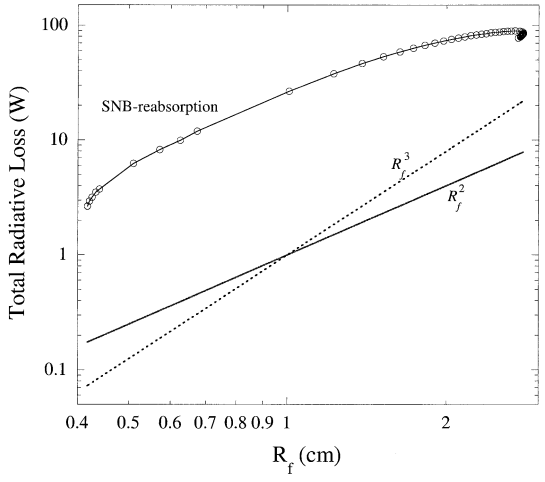

Fig. 10. Net radiative loss calculated using SNB optically thick model for flame of Fig. 8 (20%H_2-25%CH_4-55%N_2, 15.72 mg/s) as a function of flame radius (defined as location of Max T). R_f^2 and R_f^3 are plotted to compare the scaling tendency of the radiative loss.

high enough for the reactions to proceed at a sufficient rate, the overall diffusion flame structure is preserved, where fuel and oxidizer react in a thin zone in near stoichiometric proportions, globally speaking. This is because the heat release zone is much thinner than that of the encompassing radiation loss zone, as shown in Fig. 9b. Thus, the reaction zone simply sees fuel and oxidizer transported to itself at a reduced enthalpy. As the flame continues to expand, the total radiation loss increases with the increasing volume of the radiation zone until reactant leakage from reduced temperature occurs, ending in abrupt extinction. Experimental data of extended microgravity duration are needed to directly compare with computational data to better resolve the extinction phenomena.

During the flame expansion process, the total radiative heat loss rate scales roughly with the surface area ($\sim R_f^2$) and not the enclosed volume ($\sim R_f^3$) of the flame, as shown in Fig. 10. This is because the radiation heat loss zone is much thinner than the flame structure of H_2O and CO_2 products, as seen in Fig. 9a, along with the thickness of this zone increasing at a much smaller rate than that of the flame radius.

Visible Flame Luminosity

We next study the experimentally observed phenomenon of decreasing flame luminosity as the

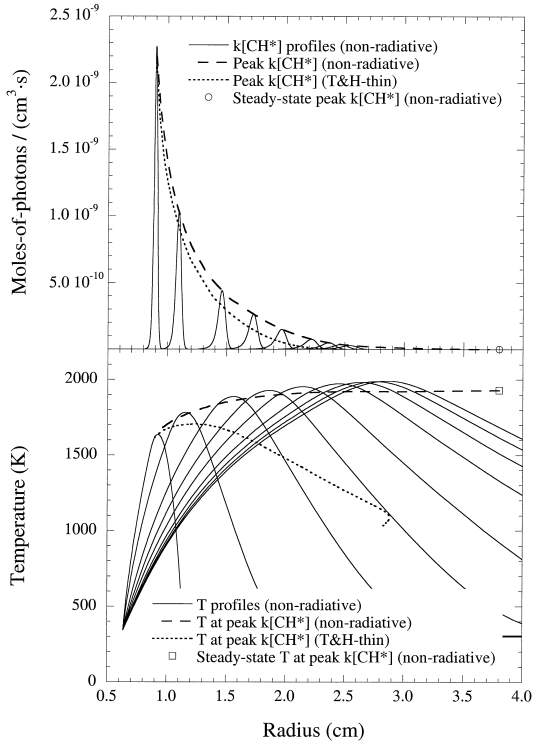

Fig. 11. Calculated peak CH* chemiluminescence and peak temperature for flame of Fig. 5 (50%H_2-10%CH_4-40%N_2, 8.1 mg/s).

flame expands with time. We first note from Fig. 11 that the simulation *without* radiative loss also predicts decreasing local luminosity from CH* with increasing flame radius. Furthermore, since the flame temperature increases with time, the decreasing luminosity is not caused by radiative heat loss. Because radiative loss reduces the mass consumption rate, as already discussed, CH* production is also reduced, resulting in less photon emission at a given flame radius, as compared to the non-radiative case. However, the overall trend of luminosity decay is the same for the non-radiative and radiative cases, as displayed in Fig. 11.

The reason for this phenomenon of local visible luminosity decay, as observed in all of the experimental flames, is mainly because of the initially enriched oxygen concentration within the reaction zone of the transient flame structure, as compared to the steady-state flame structure. That is, the initial, "squeezed," flame structure is localized into a thin, high-gradient region, as shown in the temperature profiles of

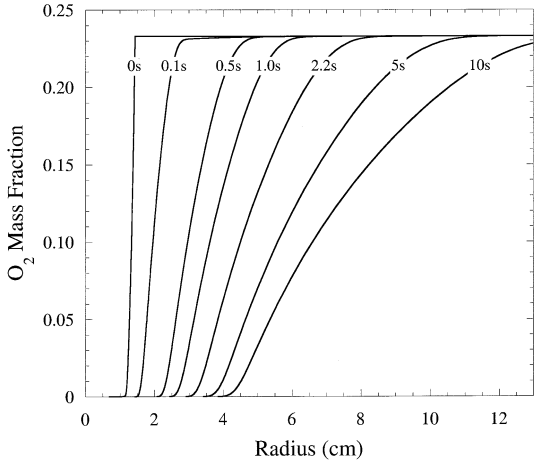

Fig. 12. Oxidizer profiles from fully transient calculations (non-radiative for flame of case [k] of Fig. 3 (50%H_2-10%CH_4-40%N_2, 13.03 mg/s). Chamber wall located at radius of 13 cm.

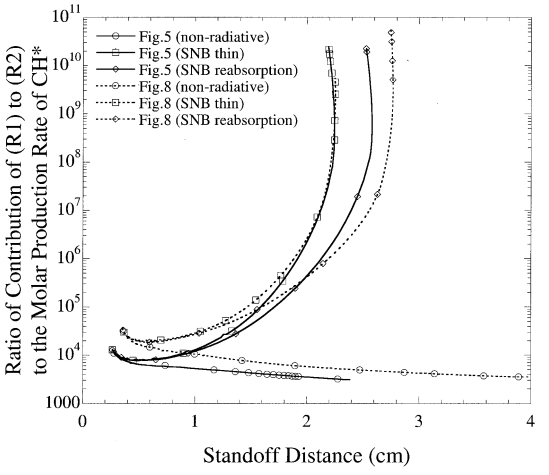

Fig. 13. Calculated contributions of the CH* production routes, (R1) and (R2), to the molar production rate of CH* for the transient flames of Fig. 5 (50%H_2-10%CH_4-40%N_2, 8.1 mg/s) and Fig. 8 (20%H_2-25%CH_4-55%N_2, 15.72 mg/s), with and without radiative heat loss.

Fig. 11. Consequently, the flux of oxidizer into the reaction zone is very large initially, and gradually subsides until it attains its steady-state value, as shown quantitatively in Fig. 12. The computations reveal that the main CH* production route for our flames is through reaction $C_2H + O_2$ (R1), rather than $C_2 + OH$ (R2), as seen in Fig. 13. Thus, increased oxygen concentration available for reaction with C_2H will result in increased chemiluminescence from CH*. The computation also confirms that the concentrations of O_2 and C_2H within the reaction zone are significantly larger because of the initial condition, as shown in Fig. 14 for the calculated O_2 and C_2H concentrations at the location of maximum CH* concentration within the flame zone. Based on the above results, it is therefore, reasonable to suggest that the decay of local luminosity of the flame is a consequence of the relaxation of the local CH* luminosity to its steady-state condition from the initial, elevated value.

A useful implication of the present result of decreasing flame luminosity is that it evinces that local visible luminosity from the flame provides no indication of either flame strength or flame extinction. In particular, Fig. 11 shows that the peak visible emission from CH* decreases rapidly despite an ever increasing flame temperature. Consequently, experimental investigations of extinction phenomena for such flames should not rely on visible observation, but rather on explicit temperature measurement. This lack of correspondence between visible luminosity and flame strength is further compounded by the ambiguity in the physical quantity represented by a "visual" observation. Specifically, the observed luminosity from the photographs represents the local flame luminosity within the field of depth in the plane of focus of the camera. In our setup, the depth-of-focus is about the diameter of the porous sphere,

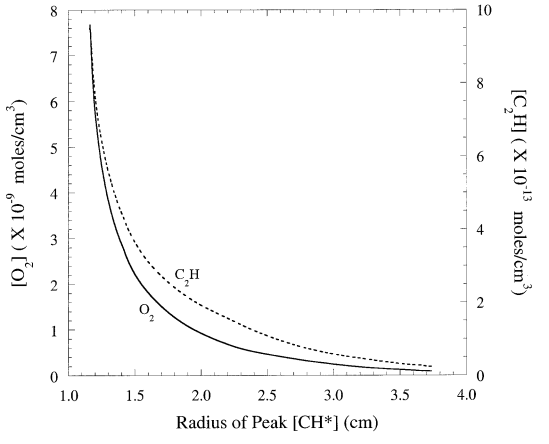

Fig. 14. Calculated (non-radiative) O_2 and C_2H concentrations at the radius of peak CH* concentration within the flame zone for the flame of Fig. 5 (50%H_2-10%CH_4-40%N_2, 8.1 mg/s).

which is much smaller than the "large" resultant microgravity flames. As such, the images neither correspond to the total photon emission from the flame or a line-of-sight projection, but more approximately to the collected light coming from a relatively thin region within the depth-of-focus, which explains why our flames appeared hollow with no luminous surface. Thus, given that the flame is always within the field-of-view of the camera lens, it is reasonable to assume that the local flame luminosity observed in the photographs is approximately proportional to the number of photons emitted per unit volume per unit time in the "plane" of symmetry and focus. Therefore, this corresponds most closely to the calculated radial CH* concentrations presented above. However, if the "visual" observation is truly comprehensive, then an integrated luminosity, corresponding to the total photon emission from CH*, that is, $\int_0^\infty 4\pi r^2 k_\tau [\mathrm{CH}^*]\mathrm{d}r$, is a more appropriate quantity. Calculations have shown that in some cases this quantity actually increases for a while before decreasing to the steady-state value.

The increasing separation distance between the peak CH* luminosity position and the peak flame temperature in the non-radiative case, shown in Fig. 5, is also the result of the "widening" structure of the flame from its initially narrow one. At the same time, however, although the reaction zone becomes thicker in physical space, the thickness of the reaction zone with respect to that of the total flame structure decreases as the flame expands toward its steady-state condition.

Boundary Effects

We now specifically examine the role of conductive heat loss to the burner on the flame properties and dynamics without radiation considerations. In the previous section, we fixed the burner temperature at the experimentally measured value for both radiative and non-radiative cases, so that there was always conductive loss to the burner. Note that the burner represents only the solid material and not the gas inside it. Ideally, the burner should be adiabatic such that all of the heat conducted toward it from the flame is directly transferred to the gas mixture within it, with its only purpose being to provide a uniform flow field. Consequently, the temperature distribution for an adiabatic burner should be the same as that for a point source issuing fuel mixture at zero radius with a temperature of 300 K. Figure 15 compares the initial temperature profiles for an adiabatic case and one where the temperature at the burner surface is fixed at 350 K. Obviously, the flame temperature is reduced due to heat loss to the burner. What is interesting, though, is that for the adiabatic case, the temperature gradient is minimal up to 0.4 cm from zero radius. Thus, if the burner were half the radius of that actually employed for this work (0.635 cm radius), then, for the same mixtures and mass flow rates, heat loss to the burner would be negligible. Nonetheless, the effect of heat loss to the burner on flame properties such as trajectory and Max T is small for the cases studied as shown in Fig. 16. Heat loss to the burner is reduced for larger flame radii, as shown in the temperature profiles of Fig. 11. Remember, though, that radiative losses are larger for larger flame radii. As the flame expands, Max T also increases for the adiabatic case, showing that this behavior is because of the enthalpic filling of the domain by the ever widening flame structure, and not to an initially reduced temperature from heat loss to the burner.

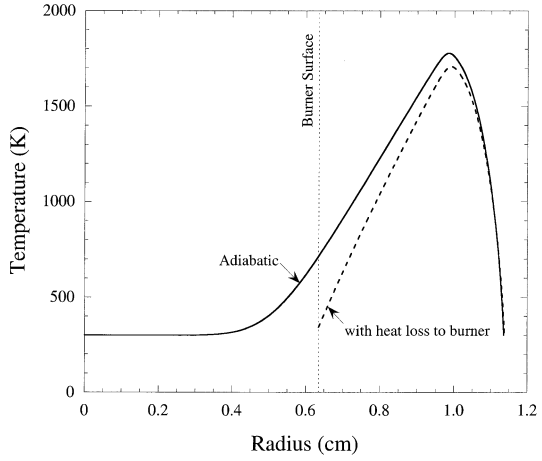

Fig. 15. Comparison of temperature profile at initial condition between adiabatic flame and flame with heat loss for case of Fig. 8 (20%H_2-25%CH_4-55%N_2, 15.72 mg/s).

We have also assessed that the effect of the chamber wall on the flame structure is minimal, for the given characteristic experimental times.

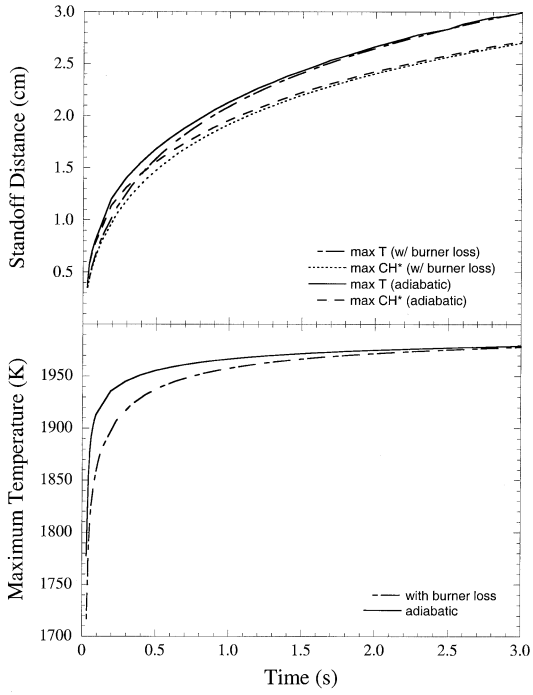

Fig. 16. (a) Flame trajectory comparison between adiabatic flame and flame with heat loss to burner. (b) Max T history comparison between adiabatic flame and flame with heat loss to burner (20%H_2-25%CH_4-55%N_2, 15.72 mg/s).

The sole purpose of the chamber is therefore to shield against flow perturbations during the experimental drop. The most convincing argument for the independence of the flame structure from the presence of the wall is from the limited "penetration" depth of oxidizer transport during the experimental transient, as revealed by the simulated oxidizer profiles of Fig. 12, for an experimental case (50%H_2/10%CH_4/40%N_2, 13.03 mg/s mass-flow rate, case (k) of Fig. 3) with the largest characteristic flame size. These calculations clearly show that the ambience near the chamber wall has not yet been affected by oxygen transport to the flame for times up to 2.2 s into the flame-spread process. Although not plotted, the "penetration" depth of temperature and all other species show similar results.

CONCLUDING REMARKS

Experimental data of good quality, spherical flames were obtained on transient diffusion flames in the 2.2-s drop tower. Experimental and computational results showed that steady-state flame behavior cannot be reached within the 2.2-s microgravity duration for the fuels and mass-flow rates tested. Fully transient computations with detailed chemistry and transport simulated well the experimental data of the flame expansion process, demonstrating that radiation with reabsorption is essential in properly capturing the flame dynamics, especially for extinction phenomena. The lack of correspondence of visible flame luminosity with the flame strength is noted, and its implication on potential misinterpretation of flame extinction in the presence of decreasing flame luminosity is suggested.

This work was supported by the NASA Microgravity Combustion Program. It is a pleasure to acknowledge useful technical discussions with and suggestions from Dr. K. Sacksteder of NASA-Glenn, Dr. L. He of Princeton University, and Prof. H. Wang of the University of Delaware.

REFERENCES

1. Atreya, A., Agrawal, S., Sacksteder, K. R., and Baum, H. R., Observations of Methane and Ethylene Diffusion Flames Stabilized Around a Blowing Porous Sphere under Microgravity Conditions, *32nd Aerospace Sciences Meeting and Exhibit*, AIAA 94-0572, 1994.
2. Atreya, A., Berhan, S., and Everest, D., Radiant Extinction of Gaseous Diffusion Flames, *Proceedings of the Fifth International Microgravity Combustion Workshop*, NASA/CP 1999-208917, 43–46 (1999).
3. Sunderland, P. B., Axelbaum, R. L., and Urban, D. L., Effects of Structure and Hydrodynamics on the Sooting Behavior of Spherical Microgravity Diffusion Flames, *Proceedings of the Fifth International Microgravity Combustion Workshop*, NASA/CP 1999-208917, 475–478 (1999).
4. Mills, K., and Matalon, M., *Combust. Sci. Technol*. 129:295–319 (1997).
5. Mills, K., and Matalon, M., *Proc. Combust. Inst*. 27: 2535–2541 (1998).
6. The Microgravity Combustion Group, *Microgravity Combustion Science: A Program Overview*, NASA TM-101424 (1989).
7. Miyasaka, K., and Law, C. K., *Proc. Combust. Inst*. 18:283–292 (1980).
8. Kumagai, S., Sakai, T., and Okajima, S., *Proc. Combust. Inst*. 13:778–785 (1970).
9. Law, C. K., Chung, S. H., and Srinivasan, N., *Combust. Flame* 38:173–198 (1980).
10. Kee, R. J., Grcar, J. F., Smooke, M. D., and Miller,

J. A., Sandia Report SAND 85-8240, Sandia National Laboratories, 1985.
11. Law, C. K., and Egolfopoulos, F. N., *Proc. Combust. Inst*. 24:137–144 (1992).
12. Tien, C. L., *Adv. Heat Transfer* 5:253–324 (1968).
13. Hubbard, G. L., and Tien, C. L., *ASME J. Heat Transfer* 100:235–239 (1978).
14. Ju, Y., Guo, H., Liu, F., and Maruta, K., *J. Fluid Mech*. 379:165–190 (1999).
15. Malkmus, W., *J. Opt. Soc. Am*. 57:323–329 (1967).
16. Soufinani, A., and Taine, J., *Int. J. Heat Mass Trans*. 40:987–991 (1997).
17. Frenklach, M., Wang, H., Yu, C.-L., Goldenberg, M., Bowman, C. T., Hanson, R. K., Davidson, D. F., Chang, E. J., Smith, G. P., Golden, D. M., Gardiner, W. C., and Lissianski, V., http://www.me.berkeley.edu/gri_mech/.
18. Hwang, S. M., Gardiner, W. C., Jr., Frenklach, M., and Hidaka, Y., *Combust. Flame* 67:65–75 (1987).
19. Porter, R. P., Clark, A. H., Kaskan, W. E., and Browne, W. E., *Proc. Combust. Inst*. 11:907–917 (1967).
20. Miller, J. A., and Melius, C. F., *Combust. Flame* 91:21–39 (1992).
21. Hwang, S. M., Gardiner, W. C., Jr., and Warnatz, J., *Prog. Aeronaut. Astronaut*. 95:198 (1984).
22. Becker, K. H., Brenig, H. H., and Tataczyk, T., *Chem. Phys. Lett*. 71:242 (1980).
23. Frenklach, M., Wang, H., and Rabinowitz, J., *Prog. Energy Combust. Sci*. 18:47–73 (1992).
24. Ju, Y., Masuya, G., and Ronney, P. D., *Proc. Combust. Inst*. 27:2619–2626 (1998).

Received 6 March 2000; revised 13 March 2001; accepted 21 March 2001